Feel free to get in contact: geo.david.fernandez@gmail.com

Is the Suez Rift in its post-rift phase?

D. Fernández-Blanco[1,2], G. de Gelder[3], and C. A-L. Jackson[2,4]

[1]*Laboratory of Marine Geophysics and Georesources, Institute of Deep-Sea Science and Engineering, Chinese Academy of Sciences, Sanya 57200, China (geo.david.fernandez@gmail.com)*

[2]*Landscape and Basins Research Group (LBRG), Department of Earth Science and Engineering, Imperial College, London, SW7 2BP, UK*

[3]*ISTerre, CNRS, Université Grenoble Alpes, France*

[4]*WSP UK Ltd, 8 First St, Manchester, M15 4RP, UK*

ABSTRACT

Failed rifts are widely assumed to enter post-rift quiescence after termination of intracontinental rifting. However, this remains largely untested and a comprehensive evaluation of the rates and patterns of post-rift tectonic (in)activity is lacking. Our novel, rift-scale geomorphic analysis reveals "post-rift" rifting across the archetypal failed rift of Suez, in Egypt. Stacked topographic swaths and river profiles document pervasive normal fault offsets in Plio-Quaternary rocks along the rift length, with fluvial metrics showing steep gradients consistent with active and young faulting. Quaternary shorelines uplifted along both margins constrain normal fault footwall uplift rates of up to 0.13±0.04 mm/yr, comparable to those of the Basin and Range, USA. This evidence of active extension in the Suez Rift, occurring after its presumed Pliocene failure, should motivate reevaluation of the tectonic activity in other "failed" rifts and of conceptual models of continental rift evolution.

INTRODUCTION

Failed rifts, or aulacogens, are tectonically inactive intracontinental basins formed where lithospheric thinning by faulting halts before full oceanic spreading (Burke, 1977). Rifting fails due to changes in plate motion, mantle dynamics and/or preferential fault relocalization at triple junctions (Sengör and Burke, 1978). The subsequent post-rift phase of thermal subsidence leads to sedimentary infill of these elongated troughs during a period of tectonic quiescence sustained by regional force balance (Buiter et al., 2023; Brune et al., 2023).

The intracontinental Suez Rift, Egypt (Fig. 1) is thought to represent a key global example of a failed rift (Patton et al., 1994). Following extension and normal faulting in the Oligo-Miocene, the rift entered a phase of post-rift thermal subsidence and sedimentation in the Pliocene, as the Dead Sea Transform became the Nubian-Arabian plate boundary (Fig. 1A; Bartov et al., 1980; Steckler et al., 1988). This plate reorganization supposedly halted rifting in Suez except at its southern end, where extension and faulting persist near the junction between the Red Sea and Aqaba rifts (e.g., Moustafa and Khalil, 2020).

Scattered geological observations and subtle geophysical signals suggest tectonic activity exists beyond the Suez Rift southern end, challenging conventional views of post-rift tectonic quiescence. Plio-Quaternary normal faulting and uplifted Quaternary shorelines document recent deformation (Bosworth and Taviani, 1996; Bosworth et al., 2019), supported by widespread, low-magnitude seismicity and GPS-derived crustal movements (Mahmoud et al., 2005; Badawy et al., 2008). Renewed extension across the rift may be driven by changes in the Euler pole between Nubian and Arabian plates (Reilinger et al., 2006) and far-field stresses associated with the Afar plume (Ebinger et al., 2010). Despite these observations, a comprehensive evaluation of the spatiotemporal span, patterns, and rates of the post-rift tectonic activity is still needed.

Here, we present an original, quantitative, rift-scale analysis of post-rift tectonics in the Suez Rift (Fig. 1C). We integrate novel and widely-tested geomorphic methods (Lajoie, 1986; Snyder et al., 2000; Armijo et al. 2015) and extend them beyond their typical fault-scale application to examine the entire rift. Our analyses: (i) reveal pervasive normal faulting in Plio-Quaternary rocks, (ii) document tens of meters of Quaternary shoreline uplift along both margins, localized in the footwalls of crustal-scale, basin-bounding normal faults, and (iii) quantify tectonic activity along the entire rift length. Our quantitative evidence of extension in the putative post-rift phase challenges models of how continental rifts evolve and fail.

GEOLOGIC SETTING

The Suez Rift accommodated motion between the Arabian and Nubian plates north of the intersection between the Red Sea Rift (Cochran, 1983) and the Aqaba Transform (Fig. 1A; Ribot et al., 2021). Magma-poor rifting from the Late Oligocene to Early Miocene created a 300-km-long, 80-km-wide basin, narrowing northwestward with decreasing extension, from Sinai's southern tip to Suez city (Fig. 1B; Patton et al., 1994). Intracontinental rifting led to three structural domains, with half-graben dip polarity alternating along the rift axis (Fig 1B; e.g., Moustafa and Khalil, 2020). Block-bounding, en-echelon faults are ~10-25 km long, strike predominantly rift-parallel (i.e., NW-SE) and accommodate throws of up to a few kilometers (Colletta et al., 1988; Moustafa and El-Raey, 1993).

METHODS

We use three robust and complementary geomorphic techniques to identify and quantify active tectonics across the entire Suez Rift (Fig. 1C): (i) stacked topographic swath profiles calculated from Digital Elevation Models (DEM) at rift-scale (~30-km-wide, ~120-km-long stripes perpendicular to rift-bounding faults) and at rift margins (throughout post-rift rocks); (ii) Quaternary coral reef terraces compiled from 25 sites along both rift margins, corrected for eustatic and glacio-isostatic effects, to derive fault slip rates with quantified uncertainties; and (iii) river and chi (χ) profiles, knickpoints and channel normalized steepness indices (k_{sn}) of the largest river networks on each rift margin, extracted from DEM data. Text S1 details datasets, stacked swaths profile construction, coral reef terrace compilation, and river network analyses.

ACTIVE RIFT-CONTROLLED RELIEF AND FAULTING

The Suez Rift relief is highly asymmetric across and along strike. The consistently shallow bathymetry (<50 m) of the rift along strike contrasts with its highly variable, rift-margin topography (Fig. 2, Fig. S1, Text S2). Inactive and still-active (see below) normal faults (black and red lines in Fig. 2A-C, respectively) bound major across-rift changes in topographic gradient. Coastal mountains locally named *gebels* have asymmetric cross-rift topographies with steep, fault-bounded, gulf-facing escarpments (500 m of elevation change over ~2 km) and gentler landward slopes (spanning over ~10 km) at Abu Durba-Araba, Hammam Faraum and El Zeit (Fig. 1, 2). Northward of these *gebels*, steep escarpments and surface displacements mark the base of triangular facets in Plio-Quaternary topography (red arrow heads in Fig. 2D).

QUATERNARY UPLIFT OF RIFT MARGINS

Raised Quaternary coral reef terraces at 25 sites record differential uplift along both margins across the entire rift (Fig. 3; Table S1). Some of these coral reef terraces were previously dated (123.5±8.5 ka, MIS 5e; 409±16 ka, MIS 11c; Bosworth et al., 2019). Maximum elevations of 19±0.5 m and 42±1 m above sea level allow us to calculate maximum uplift rates of 0.13±0.04 mm/yr and 0.10±0.2 mm/yr at *gebel* centers (Fig. 3B,D). MIS 5e terraces have comparable elevations at other *gebel* centers >200 km north of the rift's southern terminus, and are only a few meters above sea level at other sites (Fig. 3A; Gvirtzmann, 1994; Plaziat et al., 1998; Bosworth et al., 2019). At Gebel El Zeit, the most complete record of MIS 5e terraces reach ~18.5±0.5 m elevation and decay parabolically down to ~6.5±0.5 m along the coast over a horizontal distance of ~80 km (Fig. 3C). Two MIS 5e terraces at Gebel Hammam Faraum have comparable maximum elevation and along-strike elevation contrasts over similar horizontal distances (Fig. 3A).

PLIO-QUATERNARY DEFORMATION AND DRAINAGE DISEQUILIBRIUM

The disequilibrium of drainage networks provide evidence for and quantify ongoing tectonics in Plio-Quaternary rocks on both rift margins (Fig. 4,S2,S3; DR4). On the western margin (Fig. 4B,D), drainages 1-3 have rift-parallel gradients in normalized steepness indices (from k_{sn} 0-25 to k_{sn} 50-75) and knickpoints where they cross small faults within the Plio-Quaternary unit. Drainages 4-9 show peak normalized channel steepness values (k_{sn} > 100) that co-locate with river knickpoint clusters in Plio-Quaternary rocks, particularly along previously documented and newly mapped, NW-SE-striking, basinward-dipping normal faults of small throw (Fig. 1C; Bosworth et al., 2020). On the eastern margin (Fig. 4A,C), drainages 1-3 have elevated normalized steepness indexes (k_{sn} > 50) throughout their linear profiles and anomalously high values for their drainage area (k_{sn} > 100) in streams draining Plio-Quaternary rocks. Drainages 4-

7 are the largest and have peak normalized steepness index values (k_{sn} > 100) in Plio-Quaternary rocks. River 4 shows a knickpoint in Plio-Quaternary rocks and high k_{sn} values downstream of basement-bounding faults (Fig. 4E). Within Plio-Quaternary rocks, rivers 5-7 show consistently high normalized steepness channel values (k_{sn} > 100) from their outlet, whereas drainages 8-15 have linear profiles with k_{sn} > 75 near the coast.

"POST-RIFT" RIFTING: EVIDENCE, RATES AND POTENTIAL CAUSES

Evidence for recent and active normal faulting in "post-rift" rocks spans 250 km along strike of both rift margins, with normal fault networks uplifting and dissecting post-rift sequences in the hanging walls of major rift-bounding faults at three structural locations; offshore, along the coast, and within Plio-Quaternary rocks.

Offshore faults uplift coastal Plio-Quaternary plains. Although the activity of these faults is partially masked by sedimentation in the basin (Gawthorpe et al., 2003), the uplift of their footwalls results in river channels with elevated normalized steepness indexes (commonly with k_{sn} > 50; often with k_{sn} > 100) for their drainage area (e.g., Wobus et al., 2006) and river knickpoints that are not caused by any mapped structure (Fig. 4E). Should the Plio-Quaternary rock strength be uniform, this evidence documents rift-wide active strain (Fig. 4B,D).

Coastal faults produce *gebels*, distinctive, short-wavelength topographic asymmetries exposing syn- and pre-rift rocks (Fig. 2A-C). A ~80-km-long, MIS 5e parabola marks the footwall displacement profile of the gebel-bounding fault at El Zeit (Fig. 3C). Based on typical normal fault aspect ratios (Dawers et al., 1993), this length implies the bounding structure has a down-dip height of ~10-15 km, and thus transects the seismogenic layer. Here, consistent uplift rates between MIS 5e (0.13±0.04 mm/yr) and MIS 11c (0.10±0.2 mm/yr) support steady deformation since ~400 ka. We infer a comparable scale and pattern for the Gebel Hammam Faraum bounding fault, from similar terrace elevation contrasts over short horizontal distance (Fig. 3A) and ~3 km of accrued fault displacement after late Middle Miocene (Gawthorpe et al., 2003). Assuming constant rates and negligible erosion, the maximum elevation of these gebels (~500 m) supports bounding fault initiation in the Pliocene, between 3.12±0.23 and 4.44±0.2 Ma, which is generally coeval with peak fault accrual during the late states of rifting and faults that remain active (Gawthorpe et al., 2003).

Maximum footwall uplift rates at gebels (MIS 5e, 0.13±0.04 mm/yr; MIS 11c, 0.10±0.2 mm/yr) match those of slowly extending continental regions, like the Basin and Range (Ellis and Barnes, 2015) and Rhine Graben (Nivière et al., 2008), and exceed the hanging wall subsidence rates of 0.02-0.08 mm/yr since 5 Ma documented for the Suez Rift (Moretti & Colletta, 1987). Without evidence for slip acceleration, this suggests regional uplift rates of ~0.05 mm/yr (Garfunkel, 1988) and elevated uplift:subsidence ratios, in turn supporting high lower crust/upper mantle viscosities (De Gelder et al., 2019). Using normal fault angles at *gebels*, reported to decrease southward from 63° to 30° (Jackson et al., 1988; Moustafa & Khalil, 2020), and assumed uplift:subsidence ratios of ~1:1-2.5 (Basin and Range, King et al., 1988; Corinth Rift, De Gelder et al., 2019), we derive slip rates of ~0.44±0.15 and ~0.65±0.2 to mm/yr and extension rates of ~0.26±0.13 to ~0.55±0.24 mm/yr (Fig. 3D). These extension rates are substantially lower than the Oligocene rates (2.0 mm/yr) and one-quarter to one-half the Miocene rates (1.0 mm/yr) reported by Bosworth et al. (2005).

Fault networks offsetting post-rift rocks are documented at and northward of south Gharib Plain (Bosworth et al., 2019), and mapped here also further north. Triangular facets mark these newly mapped faults (Fig. 1C; 2D). The systematic spatial correlation between their mapped traces, increased channel steepness and river knickpoints record their active, localized, differential vertical motion (Fig. 4A,C; Wobus et al., 2006).

Multiple potential causes may explain "post-rift" rifting in the Suez Rift. While sediment loading could enhance fault activity (e.g., De Sagazan and Olive, 2021), the lateral continuity of fault networks, their systematic dip variation, and the crustal-scale dimensions inferred from documented aspect ratios suggest deeper regional controls. GPS-derived extension rates an order of magnitude larger than our reported rates (Mahmoud et al., 2005; Fig. 3D) indicate significant off-fault strain and also support dominant regional thermal and plate boundary forces. The northwestward decrease in fault slip and extension rates could reflect a stress propagation gradient from the Afar plume (Ebinger et al., 2010). However, Mediterranean compression-driven, oblique slip (Badawy et al., 2008) and inherited structures, known to influence strain patterns in the northern Red Sea (Bosworth et al., 2019), could control local deformation in a more complex stress field. In contrast, strain localization along major faults is supported by our inferred elevated lower crustal viscosities, and a broadly coherent uplift and response along both margins suggest a dominant control by Nubian-Arabian plate motion changes (Reilinger et al., 2006).

IMPLICATIONS FOR INTRACONTINENTAL RIFT EVOLUTION

Active faulting during a period otherwise dominated by thermal subsidence in the Suez Rift invalidates a binary "active" or "failed" classification and questions conventional models of rift abandonment. Our evidence expands the known spectrum of post-rift evolution of not-passive rift margins (Buiter et al., 2022; Brune et al., 2023), documenting tectonic activity after purported rift failure. We hope our findings motivate new, hybrid models of post-rift evolution that integrate mantle dynamics, plate reorganization, and far-field stresses with inherited structures and surface processes. A global reassessment of supposedly “failed” rifts is needed to capture the full spectrum of post-rift behavior and inform new paradigms of rifts in continents.

ACKNOWLEDGEMENTS

GdG acknowledges funding from the IRD and the Manajemen Talenta BRIN fellowship program, and research permit 52/SIP.EXT/IV/FR/5/2023 provided by the Indonesian government on May 11th 2023.

REFERENCES CITED

Armijo, R., Lacassin, R., Coudurier-Curveur, A., and Carrizo, D., 2015, Coupled tectonic evolution of Andean orogeny and global climate: Earth-Science Reviews, v. 143, p. 1–35, https://doi.org/10.1016/j.earscirev.2015.01.005.

Badawy, A., Mohamed, A.M.S., and Abu-Ali, N., 2008, Seismological and GPS constraints on Sinai sub-plate motion along the Suez rift: Studia Geophysica et Geodaetica, v. 52, p. 397–412, https://doi.org/10.1007/s11200-008-0028-9.

Bartov, Y., Steinitz, G., Eyal, M., and Eyal, Y., 1980, Sinistral movement along the Gulf of Aqaba—its age and relation to the opening of the Red Sea: Nature, v. 285, p. 220–222, https://doi.org/10.1038/285220a0.

Bosworth, W., and Taviani, M., 1996, Late Quaternary reorientation of stress field and extension direction in the southern Gulf of Suez, Egypt: Evidence from uplifted coral terraces, mesoscopic fault arrays, and borehole breakouts: Tectonics, v. 15, p. 791–802, https://doi.org/10.1029/95TC03851.

Bosworth, W., Huchon, P., and McClay, K., 2005, The Red Sea and Gulf of Aden Basins: Journal of African Earth Sciences, v. 43, p. 334–378, https://doi.org/10.1016/j.jafrearsci.2005.07.020.

Bosworth, W., Taviani, M., and Rasul, N.M.A., 2019, Neotectonics of the Red Sea, Gulf of Suez and Gulf of Aqaba, in Rasul, N.M.A., and Stewart, I.C.F., eds., Geological Setting, Palaeoenvironment and Archaeology of the Red Sea: Cham, Springer International Publishing, p. 11–35, https://doi.org/10.1007/978-3-319-99408-6_2.

Bosworth, W., Khalil, S.M., Ligi, M., Stockli, D.F., and McClay, K.R., 2020, Geology of Egypt: The Northern Red Sea, in Hamimi, Z., El-Barkooky, A., Martínez Frías, J., Fritz, H., and Abd El-Rahman, Y., eds., The Geology of Egypt: Cham, Switzerland, Springer, Regional Geology Reviews, p. 243–374, https://doi.org/10.1007/978-3-030-15265-9_9.

Brune, S., Kolawole, F., Olive, J.-A., Stamps, D.S., Buck, W.R., Buiter, S.J.H., and Furman, T., 2023, Geodynamics of continental rift initiation and evolution: Nature Reviews Earth & Environment, v. 4, p. 235–253, https://doi.org/10.1038/s43017-023-00391-3.

Buiter, S.J.H., Brune, S., Keir, D., and Peron-Pinvidic, G., 2023, Rifting continents, in Duarte, J.C., ed., Dynamics of Plate Tectonics and Mantle Convection: Elsevier, p. 459–481, https://doi.org/10.1016/B978-0-323-85733-8.00016-0.

Burke, K., 1977, Aulacogens and continental breakup: Annual Review of Earth and Planetary Sciences, v. 5, p. 371–396, https://doi.org/10.1146/annurev.ea.05.050177.002103.

Cochran, J.R., 1983, A model for development of Red Sea: AAPG Bulletin, v. 67, p. 41–69, https://doi.org/10.1306/03B5ACBE-16D1-11D7-8645000102C1865D.

Colletta, B., Le Quellec, P., Letouzey, J., and Moretti, I., 1988, Longitudinal evolution of the Suez Rift structure (Egypt): Tectonophysics, v. 153, p. 221–233.

Dawers, N.H., Anders, M.H., and Scholz, C.H., 1993, Growth of normal faults: Displacement-length scaling: Geology, v. 21, no. 12, p. 1107–1110, https://doi.org/10.1130/0091-7613(1993)021<1107:GONFDL>2.3.CO;2.

De Gelder, G., Fernández-Blanco, D., Melnick, D., Duclaux, G., Bell, R.E., Jara-Muñoz, J., and Strecker, M.R., 2019, Lithospheric flexure and rheology determined by climate cycle markers in the Corinth Rift: Scientific Reports, v. 9, 4260, https://doi.org/10.1038/s41598-018-36377-1.

De Sagazan, C., and Olive, J.-A., 2021, Assessing the impact of sedimentation on fault spacing at the Andaman Sea spreading center: Geology, v. 49, no. 4, p. 447–451, https://doi.org/10.1130/G48263.1.

Ebinger, C., Ayele, A., Keir, D., Rowland, J.V., Yirgu, G., Wright, T.J., Belachew, M., Hamling, I., and Campbell, E., 2010, Length and timescales of rift faulting and magma intrusion: The Afar rifting cycle from 2005 to present: Annual Review of Earth and Planetary Sciences, v. 38, p. 439–466, https://doi.org/10.1146/annurev-earth-040809-152333.

Ellis, M.A., and Barnes, J.B., 2015, A global perspective on the topographic response to fault growth: Geosphere, v. 11, no. 4, p. 1174–1190, https://doi.org/10.1130/GES01156.1.

Garfunkel, Z., 1988, Relation between continental rifting and uplifting: Evidence from the Suez rift and northern Red Sea: Tectonophysics, v. 150, no 1–2, p. 33–49, https://doi.org/10.1016/0040-1951(88)90294-6.

Gawthorpe, R.L., Jackson, C.A.-L., Young, M.J., Sharp, I.R., Moustafa, A.R., and Leppard, C.W., 2003, Normal fault growth, displacement localisation and the evolution of normal fault populations: the Hammam Faraun fault block, Suez rift, Egypt: Journal of Structural Geology, v. 25, no. 6, p. 883–895, https://doi.org/10.1016/S0191-8141(02)00088-3.

Jackson, J.A., White, N.J., Garfunkel, Z., and Anderson, H., 1988, Relations between normal-fault geometry, tilting and vertical motions in extensional terrains: An example from the southern Gulf of Suez: Journal of Structural Geology, v. 10, no. 2, p. 155–170, https://doi.org/10.1016/0191-8141(88)90113-7.

King, G.C.P., Stein, R.S., and Rundle, J.B., 1988, The growth of geological structures by repeated earthquakes 1. Conceptual framework: Journal of Geophysical Research, v. 93, p. 13,307–13,318, https://doi.org/10.1029/JB093iB11p13307.

Kearey, P., Klepeis, K.A., and Vine, F.J., 2009, Global tectonics: Chichester, John Wiley and Sons, 496 p.

Lajoie, K.R., 1986, Coastal tectonics, *in* Wallace, R.E., ed., Active Tectonics: Washington, D.C., National Academy Press, p. 95–124.

Mahmoud, S., Reilinger, R., McClusky, S., Vernant, P., and Tealeb, A., 2005, GPS evidence for northward motion of the Sinai Block: Implications for E. Mediterranean tectonics: Earth and Planetary Science Letters, v. 238, no. 1–2, p. 217–224, https://doi.org/10.1016/j.epsl.2005.06.063.

Moretti, I., and Colletta, B., 1987, Spatial and temporal evolution of the Suez rift subsidence: Journal of Geodynamics, v. 7, no. 1–2, p. 151–168, https://doi.org/10.1016/0264-3707(87)90069-X.

Moustafa, A.R., and El-Raey, A.K., 1993, Structural characteristics of the Suez rift margins: Geologische Rundschau, v. 82, p. 101–109, https://doi.org/10.1007/BF00563273.

Moustafa, A.R., and Khalil, S.M., 2020, Structural Setting and Tectonic Evolution of the Gulf of Suez, NW Red Sea and Gulf of Aqaba Rift Systems, in Hamimi, Z., El-Barkooky, A., Martínez Frías, J., Fritz, H., and Abd El-Rahman, Y., eds., The Geology of Egypt: Cham, Springer, Regional Geology Reviews, p. 295–342, https://doi.org/10.1007/978-3-030-15265-9_8.

Patton, T.L., Moustafa, A.R., Nelson, R.A., and Abdine, S., 1994, Tectonic evolution and structural setting of the Suez Rift: Chapter 1: Part I. Type Basin: Gulf of Suez, in Landon, S.M., ed., Interior Rift Basins: American Association of Petroleum Geologists Memoir 59, p. 9–55.

Nivière, B., Bruestle, A., Bertrand, G., Carretier, S., Behrmann, J., and Gourry, J.C., 2008, Active tectonics of the southeastern Upper Rhine graben, Freiburg area (Germany): Quaternary Science Reviews, v. 27, p. 541–555, https://doi.org/10.1016/j.quascirev.2007.11.018.

Reilinger, R., et al., 2006, GPS constraints on continental deformation in the Africa-Arabia-Eurasia continental collision zone and implications for the dynamics of plate interactions: Journal of Geophysical Research: Solid Earth, v. 111, B05411, https://doi.org/10.1029/2005JB004051.

Ribot, M., Klinger, Y., Jónsson, S., Avsar, U., Pons-Branchu, E., Matrau, R., and Mallon, F.L., 2021, Active faults' geometry in the Gulf of Aqaba, southern Dead Sea Fault, illuminated by multibeam bathymetric data: Tectonics, v. 40, e2020TC006443, https://doi.org/10.1029/2020TC006443.

Sengör, A.C., and Burke, K., 1978, Relative timing of rifting and volcanism on Earth and its tectonic implications: Geophysical Research Letters, v. 5, p. 419–421, https://doi.org/10.1029/GL005i006p00419.

Snyder, N.P., Whipple, K.X., Tucker, G.E., and Merritts, D.J., 2000, Landscape response to tectonic forcing: Digital elevation model analysis of stream profiles in the Mendocino triple junction region, northern California: GSA Bulletin, v. 112, no. 8, p. 1250–1263, https://doi.org/10.1130/0016-7606(2000)112<1250:LRTTFD>2.0.CO;2.

Steckler, M.S., Berthelot, F., Lyberis, N., and Le Pichon, X., 1988, Subsidence in the Gulf of Suez: Implications for rifting and plate kinematics: Tectonophysics, v. 153, no. 1–4, p. 249–270, https://doi.org/10.1016/0040-1951(88)90019-4.

Wobus, C., Whipple, K.X., Kirby, E., Snyder, N., Johnson, J., Spyropolou, K., Crosby, B., and Sheehan, D., 2006, Tectonics from topography: Procedures, promise, and pitfalls: Geological Society of America Special Papers, v. 398, p. 55–74, https://doi.org/10.1130/2006.2398(04).

FIGURE CAPTIONS

Figure 1. Tectonic frame, structural elements and stratigraphic units of the Suez Rift. (A) Simplified plate boundary evolution in and around the Suez Rift since the Oligocene. Plates: SI-Sinai, AR-Arabia, NU-Nubia. Boundaries: SR-Suez Rift, RSR-Red Sea Ridge, DSF-Dead Sea Fault. (B) Geological and structural map showing main rift units and fault systems, overlaying EMODnet and ALOS DEM slope maps. Units and faults slightly modified from Moustafa and Khalil (2020). Newly-mapped and known intra-rift faults are in red. Accommodation zones: ZAZ-Zaafarana, MAZ-Morgan. Text S1 details map sources, re-mapping criteria, and active fault mapping. Bottom right inset shows main plate boundaries and regional active structures. (C) Locations of geomorphic objects and subsequent figures. Georeferenced files are available in the GSA Data Repository for rift units (DR1), geologic units (DR2), faults (DR3), and river networks (DR4).

Figure 2. Suez Rift relief along its axis and two displays of coastal topography in Plio-Quaternary rocks. Axial topobathymetry of the rift in the Northern Galala (A), Northern Red Sea Hills (B), Central Red Sea Hills (C). Stacked swath profiles within 30-km-wide corridors (300 swaths at ~100 m width) viewed perpendicular to the controlling normal fault systems. (D) Stacked swath view (looking N235E, 300 swaths of ~100 m width) of the Gharib Plain perpendicular to the coast, from the sea landwards. Active faults are in red and inactive faults are in black.

Figure 3. Quaternary coastal reef terraces in the Suez Rift margins. Terrace elevations in the (A) NE coast and (C) SW coast projected perpendicularly to profile a-a' (in the upper plot) and their calculated uplift rates with uncertainties (in the lower plot). (B) Map view of terrace

locations and the location of profile a-a'. Colored dots indicate Marine Isotope Stages: MIS 5e (~123.5 ± 5.5, blue), MIS 7e (~240 ± 6 ka, green), and MIS 11c (~409 ± 16 ka, orange). (D) Calculated uplift, slip and extensional rates in main coastal faults. Key locations: GHF-Gebel Hammam Faraun, GA-Gebel Araba, GEZ-Gebel El Zeit. See Text S1 and Table S1 for details on sources, compilation criteria and rate calculations.

Figure 4. River catchments, tectonic knickpoints, and k_{sn} in rift margins, and two river channel profiles in Plio-Quaternary rocks. (A-C) Main drainages and knickpoints in the east and west margin, respectively. Trunk streams (thicker lines) and tributaries are colored by catchment and numbered south to north. Thicker colored dots mark trunk knickpoints; small black dots show tributary knickpoints. (B-D) Normalized steepness index (k_{sn}) maps for the east and west margin using reference concavity $\theta_{ref} = 0.45$. Colors range from green ($k_{sn} \leq 25$) to red ($k_{sn} > 100$). All panels overlay the geological map from Figure 1D. See larger versions of these maps in Fig. S2 and Fig. S3. (E) Displays of the longest river in the eastern margin (4, blue in the bottom half of panel, including longitudinal profile (left) and χ-elevation plot (right) of the trunk (thick blue) and some streams (gray). Trunk knickpoints are triangles and the one in Plio-Quaternary rocks is labeled. Inset shows k_{sn} variations with χ along the trunk. Complete analysis in DR4.

Fernández-Blanco et al., Fig 1 – Full page width (18.5 cm)

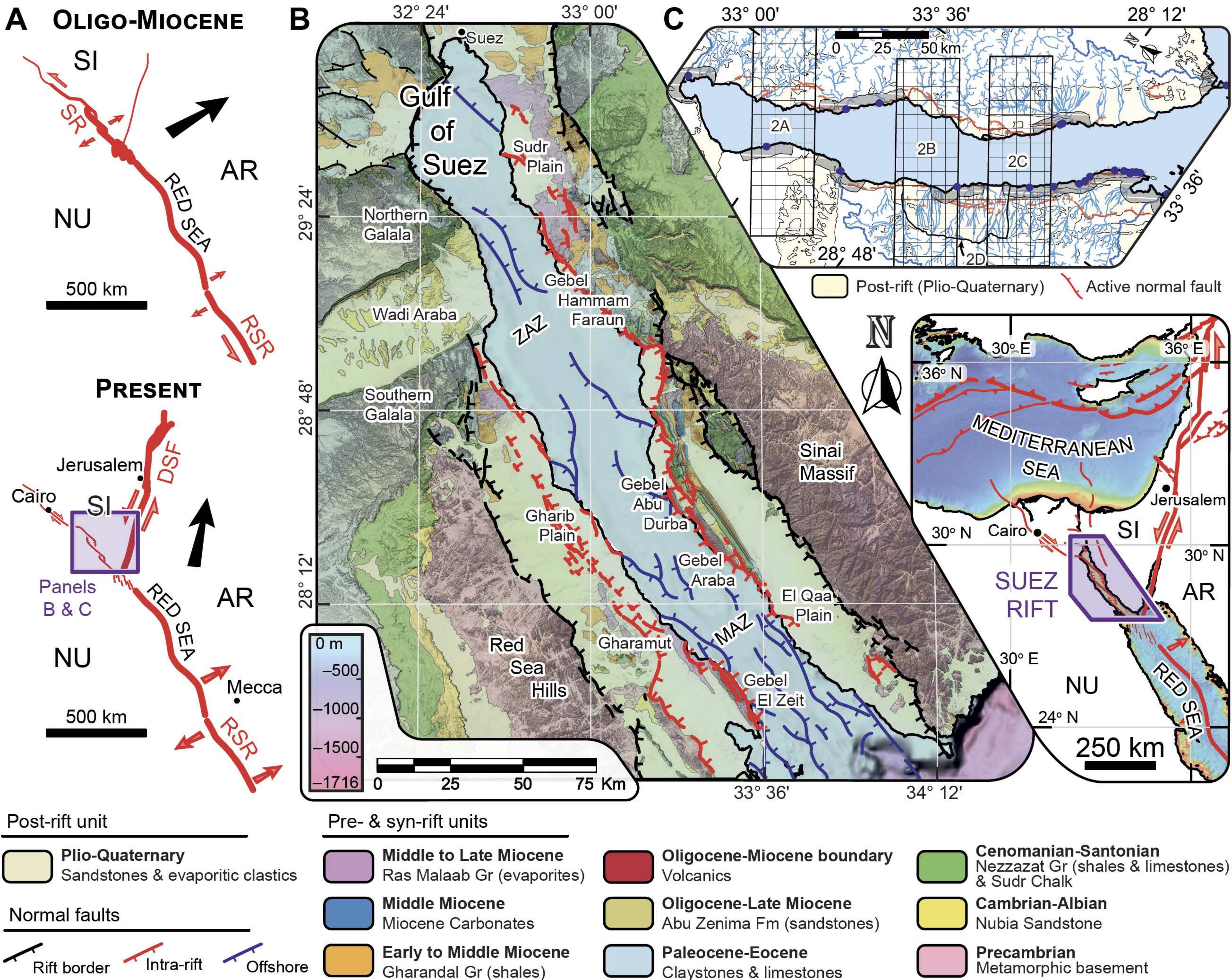

Fernández-Blanco et al., Figure 2 – Almost full page width with caption to side (14.82 cm)

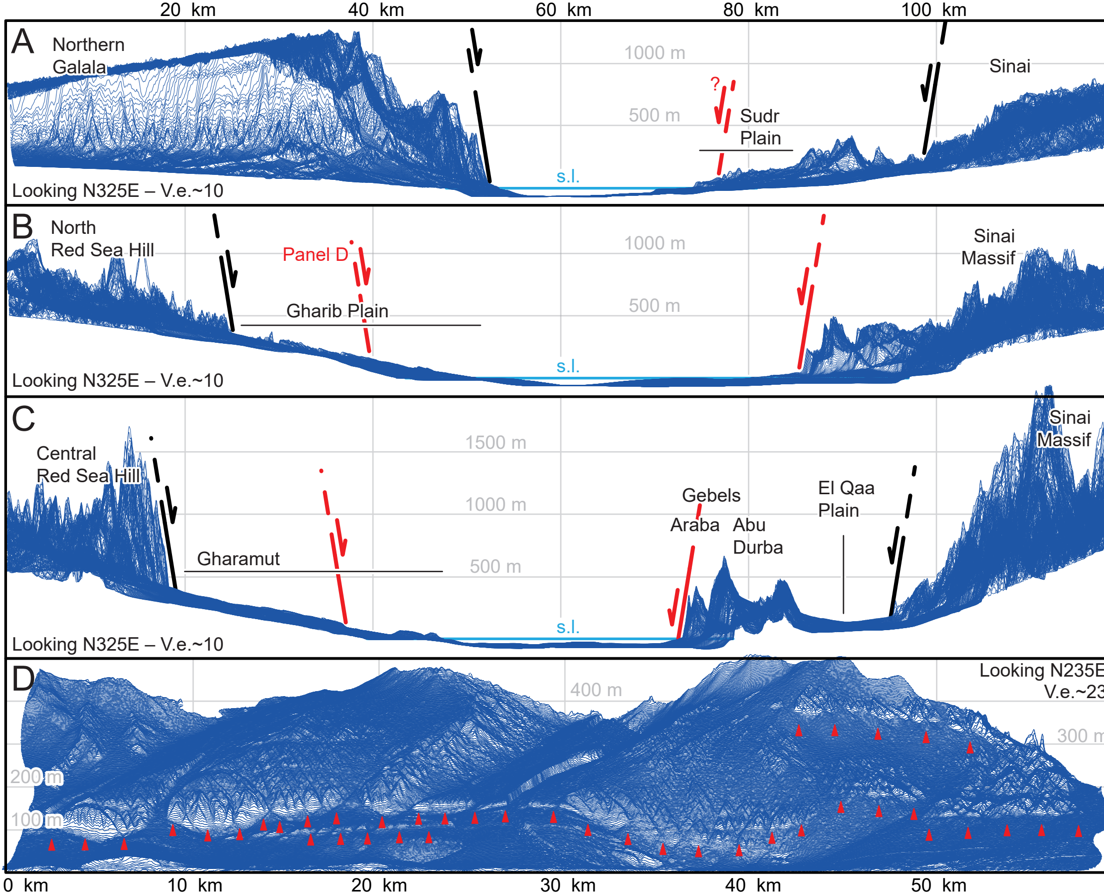

Fernández-Blanco et al., Fig 3 – 2 columns in 3-columns layout

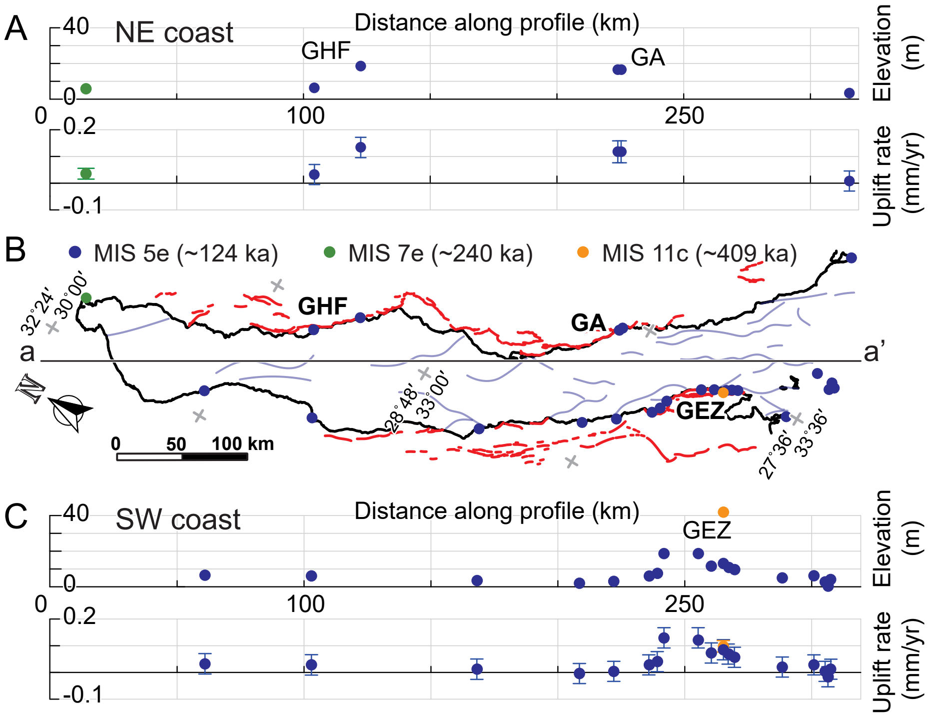

D

Gebel and fault	Max. uplift rate (mm/yr)	Fault dip (°)	Slip rate (mm/yr)	Ext. rate (mm/yr)	
				Fault	GPS
GEZ	0.13	30-42	0.65 ± 0.26	0.55 ± 0.24	–2.0
GA	0.12	40-50	0.48 ± 0.17	0.35 ± 0.15	–1.7
GHF	0.13	50-63	0.44 ± 0.15	0.26 ± 0.13	–1.2

Fernández-Blanco et al., Fig 4 – Page width (18.5 cm)

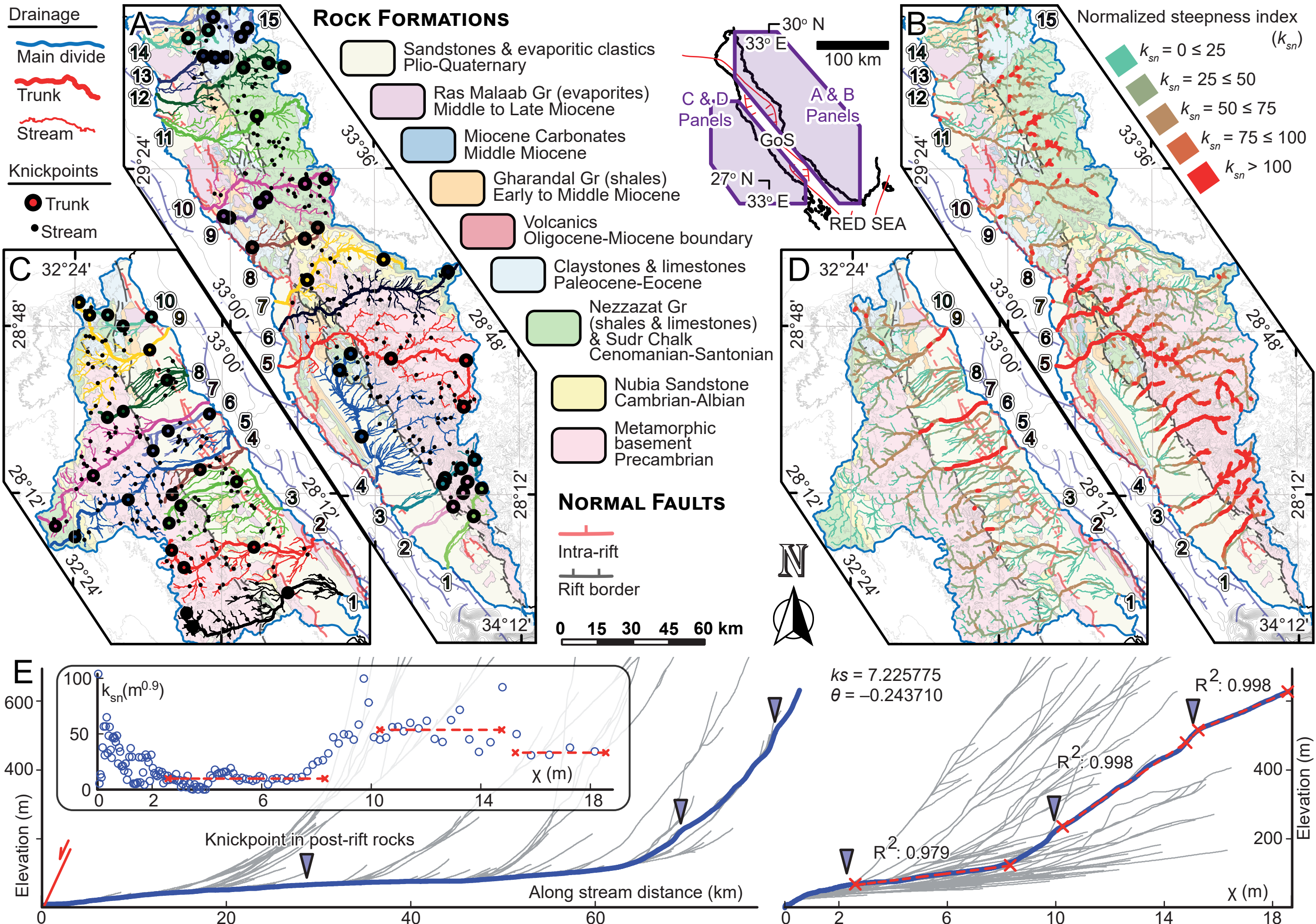

Supplementary materials for “Is the Suez Rift in a post-rift phase?”

D. Fernández-Blanco[1], G. de Gelder[2], and C. A-L. Jackson[1,3]

[1]Landscape and Basins Research Group (LBRG), Department of Earth Science and Engineering, Imperial College, London, SW7 2BP, UK (geo.david.fernandez@gmail.com)

[2]ISTerre, CNRS, Université Grenoble Alpes, France

[3]WSP UK Ltd, 8 First St, Manchester, M15 4RP, UK

TEXT S1: MATERIALS AND METHODS (CONT.)

Digital Topography and Bathymetry

For onshore areas, we used the ALOS AW3D30 Digital Surface Model (DSM) (Version 2.2, ©JAXA, https://www.eorc.jaxa.jp/ALOS/en/dataset/aw3d30/aw3d30_e.htm) of 30-m horizontal resolution. We patched small gaps and voids in the ALOS DSM with ASTER GDEM V2 (30-m horizontal resolution, ASTER, https://asterweb.jpl.nasa.gov/gdem.asp) of the same area. We filled missing values in this DEM by performing a laplacian interpolation in TopoToolbox 2 (Schwanghart and Scherler, 2014), and used the resulting DEM for all approaches with the exception of the stacked swath profiles. For the stacked swath profiles, we also used the 1/16-arc horizontal resolution offshore DEM of the EMODnet from the Bathymetry Consortium (2018, https://emodnet.ec.europa.eu/en/bathymetry), and derive an onshore-offshore composite DEM that maintains the original resolution of the onshore and offshore datasets.

Stacked Swath Topographic Profiles

The geometric analysis of topography is profusely used to study tectonic forcings (e.g., Kundu et al., 2024), including analyses on how landscapes in extensional settings evolve in relation to their controlling faults (e.g., Densmore et al., 2004). Topographic profiles have been classically used to study the geometry of topography in tectonically active regions, particularly in sectors along the strike of their controlling structures. Digital elevation data has now made possible the usage of topographic swaths, i.e., statistical representations of topography (such as minimum, maximum, and mean elevations) calculated over wide and often rectangular strips of digital elevation data. Topographic swaths present a main advantage over topographic profiles: they provide a comprehensive view of terrain characteristics that removes local particularities (e.g., Hergarten et al., 2014). Another representation of digital topography is stacked swaths, views of topography that can aid morphometric analyses over large areas of the Earth's surface. Stacked swaths are numerous parallel swath profiles, narrowly-spaced and projected perpendicular to their trend as hairlines. The latter stacked swaths result in a pseudo-3D view of topography that accentuates topographic coherence along the direction perpendicular to the point of view, highlighting sectors with similar morphology and slope. Stacked swaths allow the morphologic analysis of regional-to-tectonic scale structures, as originally shown by Armijo et al. (2015) for the coastal Andes. Stacked swaths are also a powerful approach to analyze the geometry of rifting margins in continents and the geometry of associated strain markers uplifting in extensional footwalls (De Gelder et al., 2019; Fernández-Blanco et al., 2019).

To examine the first-order structure of the Gulf of Suez along its axis, we generated stacked swath topographic profiles of the collective topobathymetry of five ~30-km wide sectors in views perpendicular to the rift-bounding fault systems. Each profile spans from one margin to the other, capturing rift-bounding faults that separate Precambrian basement from rift units or rift units from post-Miocene rocks (Fig. 2A-C, Fig. S1). We constructed each sector view by stacking 300 parallel swath profiles of averaged topography as hairlines. The width of individual swaths (~100 m) was determined dynamically by dividing the total DEM width in the projection direction by the number of swaths. This approach yields elevation averages from 4 pixels onshore and 2 pixels offshore per swath. To investigate Plio-Quaternary deformation, we extracted additional stacked swath visualizations from key sectors along both rift margins, clipping the onshore DEM within Plio-Quaternary rocks. In particular, we analyzed the Gharib Plain using 300 stacked swath profiles of ~100 m width, oriented N235°E from the coastline inland, revealing the topographic expression of recent fault activity (Fig. 2D).

River Profiles and Knickpoints

Rivers are sensitive to tectonic and climatic changes (e.g., Whipple & Tucker, 1999; Kirby & Whipple, 2012). Rivers record key information about tectonic and climatic forcing(s) that influenced or are influencing them, and the geometry of their longitudinal profiles and local convexities (knickpoints or knickzones) can be derived from DEMs and described with stream power erosion laws (e.g., Whipple & Tucker, 1999; Whipple, 2004; Wobus et al., 2006). The information recorded by rivers upstream of normal faults transecting their drainage can be used to derive normal fault growth and linkage (e.g., Whittaker, 2012; Whittaker & Walker, 2015; Roda-Boluda & Whittaker, 2016; Fernández-Blanco et al., 2019). Similarly, rivers have been used to resolve the pattern of uplift in extensional rift margins and footwalls, and the slip rates of their bounding faults (e.g., Boulton & Whittaker, 2009; Whittaker et al., 2008; Gallen & Wegmann 2017; Fernández-Blanco et al. 2019).

The functional relationship between river channel steepness normalized by upstream drainage area and the rate of erosion or rock uplift suggest that changes in the relative rate of erosion or uplift are reflected in the steepness river channels (Snyder et al., 2000; Ouimet et al., 2009; DiBiase et al., 2010). This empirical relationship is strengthened by bedrock river incision models that relate channel slope in the stream at a location, and drainage area used as a proxy for flow discharge, upstream of it

$$\frac{dz}{dt} = U - E = U - KA^{m}S^{n} \quad (1)$$

when integrating the stream power incision model for detachment-limited rivers and the law of conservation of mass. The change in elevation of the channel bed with time (dz/dt) depends on the rate of rock uplift in relation to a constant base level (*U*), stream erosion (*E*), and the drainage area upstream of a point (*A*) with a channel slope of *S*. Variables dependent of the incision process, climate, hydrology of erosion and substrate are incorporated into the dimensional coefficient K (e.g., Whipple, 2004). The positive constants of n and m are controlled by erosion processes, basin hydrology, and channel geometry (Howard, 1994; Whipple & Tucker, 1999; Tucker & Whipple, 2002).

The channel slope at a specific site can be calculated assuming steady-state conditions by which rock uplift rate is equal to erosion rate, using:

$$S = (U/K)^{1/n} A^{-(m/n)} \quad (2)$$

Eq 2 is comparable to a power-law function that defines the geometry of a longitudinal profile in equilibrium by means of upstream contributing drainage area and channel parameters (steepness and concavity indexes), i.e. Flint’s (1974) law, so that the ratio between rock uplift and substrate erodibility is proportional to the steepness index and the ratio of m to n is equal to the concavity index (Snyder et al., 2000; Kirby & Whipple, 2012).

Studies commonly derive a normalized steepness index, k_{sn}, in an attempt to remove the strong influence that river channel concavity, defined as θ or m/n, has on the steepness index. This is usually done using a fixed concavity index as a reference of ~0.45, a value that has been found in many empirical studies for a large number of graded rivers assumed to be near equilibrium (e.g., Snyder et al., 2000; Wobus et al., 2006; Kirby & Whipple, 2012). In this contribution, we calculate normalized steepness index (k_{sn}) values using a reference concavity of ~0.45 to compare relative patterns of rock uplift among different drainages. The calculation of k_{sn} by linear regression of *log S* and *log A* (Kirby & Whipple, 2012) introduces unwanted noise in the data that we avoid by using the integral method of Perron and Royden (2013), i.e. the χ method for river profiles. This analysis uses χ as an integral quantity in length units, derived by a transformation from the horizontal coordinate (distance) of the river profile.

$$z(x) = z(x_b) + \left(\frac{U}{K}\right)^{\frac{1}{n}} \int_{x_b}^{x} \frac{dx}{A(x)^{m/n}} \qquad (3)$$

$$z(x) = z(x_b) + \left(\frac{U}{KA_o^m}\right)^{\frac{1}{n}} \chi \qquad (4)$$

with:

$$\chi = \int_{x_b}^{x} \left(\frac{A_o}{A(x)}\right)^{m/n} \qquad (5)$$

Eq 4 is a linear equation, with a gradient of $(U/KA_o{}^m)^{1/n}$, an y-intercept of $z(x_b)$, and z and χ are the dependent and independent variables, respectively. This allows for *χ-plots* of χ vs z, where rivers in steady-state appear as straight lines. The standardization of *χ-plots* can be done assuming that A_o is 1, thereby doing the slope of a river in a *χ-plot* is the same as k_{sn} (e.g., Gallen & Wegmann, 2017).

Rivers that are affected by a change in rock uplift rate develop convexities in their longitudinal profiles known as knickpoints. Knickpoints behave as a kinematic-wave that steepens the river channels as they migrate upstream (Rosenbloom & Anderson, 1994). During their upstream migration, knickpoints act like boundaries separating two graded sectors of a river profile; an upstream sector that is unaffected by the change in uplift rate and a downstream sector that is adjusted or adjusting to it (e.g., Whipple & Tucker, 1999; Snyder et al., 2000).

We used TopoToolbox 2 (Schwanghart & Scherler, 2014) in conjunction with the χ Profiler package (Gallen & Wegmann, 2017) for all the analysis of fluvial topography. For example, the former was used to derive the flow direction and extract the river profiles, and the latter to perform the river profile analysis and plot k_{sn} and χ values. We clipped the onshore DEM with the drainage area of rivers discharging into the gulf from both rift margins. We manually delineated drainage areas on the few occasions where automatic methods failed to reproduce them. We calculated the flow direction of river networks with TopoToolbox 2, using the option “fill” for fluvial channels with drainage areas $\geq 10^6$ m^2, i.e. removing the potential effect of debris-flow processes (e.g., Stock & Dietrich, 2003). We derived fluvial longitudinal profiles using *Ao* = 1 and *m/n* = 0.45, and a moving window average of 500 m, aimed at reducing noise in the DEM and effects related to local variations, and thus out of the scope of this contribution. We picked up knickpoints manually for the 15 largest river networks in each rift margin.

Normalized Steepness Index (k_{sn})

We derived χ and k_{sn} values for rivers in both margins of the Suez Rift. Same as for the river longitudinal profiles, we calculated χ and k_{sn} values with the χ Profiler package (Gallen & Wegmann, 2017) for fluvial channels with draining areas $\geq 10^6$ m^2 using Ao = 1 and m/n = 0.45, and removed all streams <1 km. We binned normalized steepness index (k_{sn}) values in groups of 25 (0 to <= 25; 25 to <= 50; …) aimed to be representative but containing different quantities of stream sectors of similar length. The total number of stream sectors decreases with higher k_{sn} values, with 0-25 and 25-50 having roughly 3800 stream sectors, 50-75 having about half, and 75-100 and >100 having roughly a quarter of that.

Uplifted Marine Terraces

Marine terraces are relatively flat or gently inclined surfaces of marine origin, bounded by steeper slopes seaward and landward (Pirazzoli, 2005). In subtropical areas, like in the Gulf of Suez, they often result from bioconstruction by coral reefs. Marine terraces typically form during the highest peaks of sea-level oscillations, i.e. at sea-level highstands (Lajoie, 1986). Marine terraces develop relatively close to sea-level and thus can be used as “palaeo-geodetic” strain markers to quantify deformation since their formation (e.g., De Gelder et al., 2015; Merritts and Bull, 1989). In rifts and normal fault systems, marine terraces are typically used to derive footwall uplift rates, and in turn to constrain fault geometry (e.g., Bell et al., 2017) or fault slip rate estimates (e.g., Armijo et al. 1996; De Gelder et al., 2019; Robertson et al., 2019), as we do in this contribution.

We estimate coastal uplift rates compiling locations, elevations and ages of coral reef terrace data described by previous studies along the Suez Rift coast (Supplementary Table S1; Gvirtzman, 1994; Bosworth and Taviani, 1996; Plaziat et al., 1998; Bosworth et al., 2019). The 25 isolated outcrops occur along both NE and SW coasts, commonly in the footwalls of mapped normal faults. Locations are based on published maps, and accurate within a few kilometers. Suez Rift terrace ages are restricted to past sea-level highstands, specifically Marine Isotope Stages (MIS) 5e, 7e and 11c. We calculate the uplift rate U at different locations using U = (HT - HSL)/T, where T is the age of terrace formation, and HT is the present elevation above modern mean sea-level, and HSL is the relative sea-level elevation at the time of terrace formation. Following Gallen et al. (2014), we calculate standard errors, SE, as:

$$SE(u)^2 = u^2\left(\left(\frac{{\sigma_H}^2}{(H_T - H_{SL})^2}\right) + \left(\frac{{\sigma_T}^2}{T^2}\right)\right)$$

where σH is the uncertainty result of combining (i) terrace elevation, as described within the compiled literature, (ii) eustatic sea-level elevation during the time of terrace formation, and (iii) Glacio-Isostatic Adjustments (GIA) for the location of the Suez Rift. As eustatic sea-level correction for MIS 5e, MIS 7e and MIS 11c we use 5.5±3.5 m, 0.5±3.5 m, and 5±8 m (Murray-Wallace and Woodroffe, 2014), respectively, and as GIA estimate we take the range of -3±3 m suggested by models of Lambeck et al. (2011) for MIS 5e. No GIA-corrections have been proposed in literature for MIS 7 and MIS 9, and we assume those to be similar to MIS 5e. For the age of terrace formation T and corresponding uncertainties σT we use 123.5±8.5 ka, 240±6 ka, and 409±16 ka for MIS 5e, MIS 7e, and MIS 11c, respectively (Masson-Delmotte et al., 2010). We expect that the additional uncertainty in uplift rate derived from the precise depth of coral reef terrace formation is relatively minor with respect to other factors (see discussion in Bosworth et al., 2019).

TEXT S2: DETAILS ON MAPS IN FIGURE 1

Here we provide details on the maps shown in Figure 1, including details on the data used, the criteria to remap of units and structures shown in Fig. 8.7 of Moustafa and Khalil (2020), and the procedure to map new active faults.

The regional tectonic context in Panel (B) incorporates boundaries from Flerit et al. (2004) and Masson et al. (2015) for areas north of Jerusalem, and Courtillot et al. (1987) for southern regions. The base maps in panels (C) and (D) combine multiple data sources, as detailed in the *Digital Topography and Bathymetry* section above. We processed this topographic data using Global Mapper v15 to generate multiple visualization products for structural interpretation and digitized and mapped geologic objects using MAPPublisher® (Avenza System Inc.).

We digitized the geological and structural map presented in Fig. 8 of Moustafa and Khalil (2020), and employed complementary visualization techniques to increase its accuracy when possible. For this, we used grayscale hillshade maps with a primary sunlight azimuth of 45° at four directional intervals (90° intervals), starting from N145°E, which is the overall rift orientation. We also calculated and plotted elevation contours at 200-m intervals, with emphasis on the 1-km contour, to help highlight major topographic transitions. We combined these maps with slope and colored shade maps for a thorough terrain analysis, in which we modified geological contacts where the slope gradient mismatched previously mapped lithological boundaries. Similarly, we shifted fault locations on the basis of clear evidence of displaced topography in the high-resolution terrain analysis. Our modifications were systematically small, reflecting the overall quality of the original map (Moustafa and Khalil, 2020).

We mapped active faults following a three-tier hierarchical classification based on estimated relief displacement. These active faults are marked with red lines of varying thickness that correlate to estimated displacement magnitude. Systematic analysis of slope breaks, relief displacement patterns, and abrupt topographic changes guided the identification of active structures, distinguishing them from the inherited structural framework. We reviewed the map of active faults for improved accuracy using additional constraints from the other analyses presented in this contribution.

The GSA Data Repository contains all georeference files for rift units (DR1), geologic units (DR2), faults (DR3), and river networks and their analyses (DR4), as well as the merged DEM (DR5).

FIGURE S1: SUEZ RIFT RELIEF ALONG ITS AXIS

Axial topobathymetry of the rift in the Northern and Southern Galala (A and B) and Northern, Central and Southern Red Sea Hills (C, D and E). Stacked swath profiles contain 300 swaths of ~100 m width inside 30-km-wide corridors that are perpendicular to the controlling normal fault systems.

FIGURE S2: RIVERS EAST MARGIN

(A) Map of main drainages and their knickpoints in the western rift margin. Different river drainages are shown with different colors and numerated starting from the south. Trunks are highlighted with thicker strokes. Knickpoints in the trunks are shown as larger, thicker-stroke dots colored as their drainages, whereas knickpoints in the rest of the streams are represented with small black dots. (B) Map of normalized channel steepness indexes (k_{sn}) (with reference concavity, $\theta ref = 0.45$) in the eastern rift margin. Index values are grouped into five groups and shown in cold to hot colors as values increase. Both panels are overlaying the geology and structural map of Fig. 1.

FIGURE S3: RIVERS WEST MARGIN

(A) Map of main drainages and their knickpoints in the western rift margin. Different river drainages are shown with different colors and numerated starting from the south. Trunks are highlighted with thicker strokes. Knickpoints in the trunks are shown as larger, thicker-stroke dots colored as their drainages, whereas knickpoints in the rest of the streams are represented with small black dots. (B) Map of normalized channel steepness indexes (k_{sn}) (with reference concavity, $\theta ref = 0.45$) in the western rift margin. Index values are grouped into five groups and shown in cold to hot colors as values increase. Both panels are overlaying the geology and structural map of Fig. 1.

TABLE S1: CORAL REEF TERRACES COMPILATION

Compiled data from Gvirtzmann, 1994 (Gv), Plaziat et al., 1998 (Pl) and Bosworth et al., 2019 (Bo), the latter being largely based on the data of Bosworth and Tavani, 1996. Details on uplift rate and uncertainty calculation can be found in the MATERIALS AND METHODS (CONT.) section within the Supplementary Material.

Site	X coord.	Y coord.	Level	Age (ka)	Elevation (m)	Uplift Rate (mm/yr)	Source
SE-Islands	577148	3048006	MIS 5e	123.5 ± 5.5	4 ± 0.5	0.01 ± 0.04	Bo
SE-Islands	575624	3049438	MIS 5e	123.5 ± 5.5	3 ± 0.5	0.00 ± 0.04	Bo
SE-Islands	578395	3049761	MIS 5e	123.5 ± 5.5	0.5 ± 0.5	-0.02 ± 0.04	Bo
SE-Islands	578625	3056456	MIS 5e	123.5 ± 5.5	6 ± 0.5	0.03 ± 0.04	Bo
SE-Islands	558171	3058211	MIS 5e	123.5 ± 5.5	5 ± 0.5	0.02 ± 0.04	Bo
Gebel El Zeit	557248	3079404	MIS 5e	123.5 ± 5.5	9.5 ± 0.5	0.06 ± 0.04	Bo
Gebel El Zeit	556232	3081436	MIS 5e	123.5 ± 5.5	11 ± 0.5	0.07 ± 0.04	Bo
Gebel El Zeit	554409	3082833	MIS 11c	409 ± 16	42 ± 1	0.10 ± 0.02	Bo
Gebel El Zeit	554986	3083190	MIS 5e	123.5 ± 5.5	13 ± 0.5	0.09 ± 0.04	Bo
Gebel El Zeit	552861	3087345	MIS 5e	123.5 ± 5.5	11.5 ± 0.5	0.07 ± 0.04	Bo
Gebel El Zeit	550276	3091640	MIS 5e	123.5 ± 5.5	18.5 ± 0.5	0.13 ± 0.04	Bo
Gebel El Zeit	539656	3100828	MIS 5e	123.5 ± 5.5	18.5 ± 0.5	0.13 ± 0.04	Bo
Gebel El Zeit	536055	3101658	MIS 5e	123.5 ± 5.5	7.5 ± 0.5	0.04 ± 0.04	Bo
Gebel El Zeit	533054	3103505	MIS 5e	123.5 ± 5.5	6 ± 0.5	0.03 ± 0.04	Bo
Gharamut	523773	3113941	MIS 5e	123.5 ± 5.5	3 ± 0.5	0.00 ± 0.04	Bo
Gharamut	515826	3124624	MIS 5e	123.5 ± 5.5	2 ± 0.5	0.00 ± 0.04	Bo
Gharib Plain	493318	3157457	MIS 5e	123.5 ± 5.5	4 ± 1	0.01 ± 0.04	Pl
Wadi Araba	463860	3214894	MIS 5e	123.5 ± 5.5	6 ± 1	0.03 ± 0.04	Pl

N-Galala	451486	3255895	MIS 5e	123.5 ± 5.5	6.5 ± 1	0.03 ± 0.04	Pl
SE-Cape	623615	3068069	MIS 5e	123.5 ± 5.5	3.5 ± 0.5	0.01 ± 0.04	Bo
Gebel Araba	555078	3129870	MIS 5e	123.5 ± 5.5	17 ± 2	0.12 ± 0.04	Gv
Gebel Araba	553693	3130563	MIS 5e	123.5 ± 5.5	17 ± 2	0.12 ± 0.04	Gv
Gebel HF	506522	3218774	MIS 5e	123.5 ± 5.5	19 ± 0.5	0.13 ± 0.04	Bo
Gebel HF	493317	3231818	MIS 5e	123.5 ± 5.5	6.5 ± 0.5	0.03 ± 0.04	Bo
Suez	458412	3314487	MIS 7e	240 ± 6	6.0 ± 1.5	0.04 ± 0.02	Pl

REFERENCES CITED (in Supplementary Material)

Armijo, R., Lacassin, R., Coudurier-Curveur, A., and Carrizo, D., 2015, Coupled tectonic evolution of Andean orogeny and global climate: Earth-Science Reviews, v. 143, p. 1–35, https://doi.org/10.1016/j.earscirev.2015.01.005.

Armijo, R., Meyer, B., King, G.C.P., Rigo, A., and Papanastassiou, D., 1996, Quaternary evolution of the Corinth Rift and its implications for the Late Cenozoic evolution of the Aegean: Geophysical Journal International, v. 126, no. 1, p. 11–53, https://doi.org/10.1111/j.1365-246X.1996.tb05264.x.

Bell, R.E., Duclaux, G., Nixon, C.W., Gawthorpe, R.L., and McNeill, L.C., 2017, High-angle, not low-angle, normal faults dominate early rift extension in the Corinth Rift, central Greece: Geology, v. 46, p. 115–118, https://doi.org/10.1130/G39560.1.

Bosworth, W., and Taviani, M., 1996, Late Quaternary reorientation of stress field and extension direction in the southern Gulf of Suez, Egypt: Evidence from uplifted coral terraces, mesoscopic fault arrays, and borehole breakouts: Tectonics, v. 15, p. 791–802, https://doi.org/10.1029/95TC03851.

Bosworth, W., Taviani, M., and Rasul, N.M.A., 2019, Neotectonics of the Red Sea, Gulf of Suez and Gulf of Aqaba, in Rasul, N.M.A., and Stewart, I.C.F., eds., Geological Setting, Palaeoenvironment and Archaeology of the Red Sea: Cham, Springer International Publishing, p. 11–35, https://doi.org/10.1007/978-3-319-99408-6_2.

Boulton, S.J., and Whittaker, A.C., 2009, Quantifying the slip rates, spatial distribution and evolution of active normal faults from geomorphic analysis: Field examples from an oblique-extensional graben, southern Turkey: Geomorphology, v. 104, no. 3–4, p. 299–316, https://doi.org/10.1016/j.geomorph.2008.09.007.

Courtillot, V., Armijo, R., and Tapponnier, P., 1987, Kinematics of the Sinai triple junction and a two-phase model of Arabia-Africa rifting: Geological Society, London, Special Publications, v. 28, no. 1, p. 559–573, https://doi.org/10.1144/GSL.SP.1987.028.01.37.

De Gelder, G., Fernández-Blanco, D., Lacassin, R., Armijo, R., Delorme, A., Jara-Muñoz, J., and Melnick, D., 2015, Corinth terraces re-visited: Improved paleoshoreline determination using Pleiades-DEMs, in DRT: 20th International Conference on Deformation Mechanisms, Rheology and Tectonics: Aachen, Germany, v. 97, p. 12–14, https://doi.org/10.1127/1864-5658/2015-06.

De Gelder, G., Fernández-Blanco, D., Melnick, D., Duclaux, G., Bell, R.E., Jara-Muñoz, J., and Strecker, M.R., 2019, Lithospheric flexure and rheology determined by climate cycle markers in the Corinth Rift: Scientific Reports, v. 9, 4260, https://doi.org/10.1038/s41598-018-36377-1.

Densmore, A.L., Dawers, N.H., Gupta, S., Guidon, R., and Goldin, T., 2004, Footwall topographic development during continental extension: Journal of Geophysical Research, v. 109, F03001, https://doi.org/10.1029/2003JF000115.

DiBiase, R.A., Whipple, K.X., Heimsath, A.M., and Ouimet, W.B., 2010, Landscape form and millennial erosion rates in the San Gabriel Mountains, CA: Earth and Planetary Science Letters, v. 289, no. 1–2, p. 134–144, https://doi.org/10.1016/j.epsl.2009.10.036.

EMODnet Bathymetry Consortium, 2018, EMODnet Digital Bathymetry (DTM): Available at https://sextant.ifremer.fr/record/18ff0d48-b203-4a65-94a9-5fd8b0ec35f6/ (accessed September 2019).

Fernández-Blanco, D., de Gelder, G., Lacassin, R., and Armijo, R., 2019, A new crustal fault formed the modern Corinth Rift: Earth-Science Reviews, v. 199, no. 102919, https://doi.org/10.1016/j.earscirev.2019.102919.

Fernández-Blanco, D., de Gelder, G., Lacassin, R., and Armijo, R., 2019, Geometry of flexural uplift by continental rifting in Corinth, Greece: Tectonics, v. 39, e2019TC005685, https://doi.org/10.1029/2019TC005685.

Flerit, F., Armijo, R., King, G., and Meyer, B., 2004, The mechanical interaction between the propagating North Anatolian Fault and the back-arc extension in the Aegean: Earth and Planetary Science Letters, v. 224, no. 3–4, p. 347–362, https://doi.org/10.1016/j.epsl.2004.05.028.

Flint, J.J., 1974, Stream gradient as a function of order, magnitude, and discharge: Water Resources Research, v. 10, no. 5, p. 969–973, https://doi.org/10.1029/WR010i005p00969.

Gallen, S.F., and Wegmann, K.W., 2017, River profile response to normal fault growth and linkage: An example from the Hellenic forearc of south-central Crete, Greece: Earth Surface Dynamics, v. 5, no. 1, p. 161–186, https://doi.org/10.5194/esurf-5-161-2017.

Gallen, S.F., Wegmann, K.W., Bohnenstiehl, D.R., Pazzaglia, F.J., Brandon, M.T., and Fassoulas, C., 2014, Active simultaneous uplift and margin-normal extension in a forearc high, Crete, Greece: Earth and Planetary Science Letters, v. 398, p. 11–24, https://doi.org/10.1016/j.epsl.2014.04.038.

Gvirtzman, G., 1994, Fluctuations of sea level during the past 400,000 years: The record of Sinai, Egypt (northern Red Sea): Coral Reefs, v. 13, p. 203–214, https://doi.org/10.1007/BF00303633.

Hergarten, S., Robl, J., and Stüwe, K., 2014, Extracting topographic swath profiles across curved geomorphic features: Earth Surface Dynamics, v. 2, p. 97–104, https://doi.org/10.5194/esurf-2-97-2014.

Howard, A.D., 1994, A detachment-limited model of drainage basin evolution: Water Resources Research, v. 30, no. 7, p. 2261–2285, https://doi.org/10.1029/94WR00757.

Kirby, E., and Whipple, K.X., 2012, Expression of active tectonics in erosional landscapes: Journal of Structural Geology, v. 44, p. 54–75, https://doi.org/10.1016/j.jsg.2012.07.009.

Kundu, B., Zwaan, F., and Senapati, B., 2024, Unfolding rotational tectonics and topographic evolution from localized versus diffuse plate boundary counterparts: Scientific Reports, v. 14, 8199, https://doi.org/10.1038/s41598-024-58921-y.

Lajoie, K.R., 1986, Coastal tectonics, in Wallace, R.E., ed., Active Tectonics: Washington, D.C., National Academy Press, p. 95–124.

Lambeck, K., Antonioli, F., Purcell, A., and Silenzi, S., 2011, Sea level change along the Italian coast during the Holocene and projections for the future: Quaternary International, v. 232, p. 250–257, https://doi.org/10.1016/j.quaint.2010.04.026.

Merritts, D., and Bull, W.B., 1989, Interpreting Quaternary uplift rates at the Mendocino triple junction, northern California, from uplifted marine terraces: Geology, v. 17, p. 1020–1024, 10.1130/0091-7613(1989)017<1020:IQURAT>2.3.CO;2.

Masson-Delmotte, V., Stenni, B., Jouzel, J., and members of the EPICA community, 2010, EPICA Dome C record of glacial and interglacial intensities: Quaternary Science Reviews, v. 29, p. 113–128, https://doi.org/10.1016/j.quascirev.2009.09.030.

Masson, F., Hamiel, Y., Agnon, A., Klinger, Y., and Deprez, A., 2015, Variable behavior of the Dead Sea Fault along the southern Arava segment from GPS measurements: Comptes Rendus Geoscience, v. 347, no. 4, p. 161–169, https://doi.org/10.1016/j.crte.2014.11.001.

Moustafa, A.R., and Khalil, S.M., 2020, Structural Setting and Tectonic Evolution of the Gulf of Suez, NW Red Sea and Gulf of Aqaba Rift Systems, in Hamimi, Z., El-Barkooky, A., Martínez Frías, J., Fritz, H., and Abd El-Rahman, Y., eds., The Geology of Egypt: Cham, Springer, Regional Geology Reviews, p. 295–342, https://doi.org/10.1007/978-3-030-15265-9_8.

Murray-Wallace, C.V., and Woodroffe, C.D., 2014, Quaternary sea-level changes: A global perspective: Cambridge, Cambridge University Press, 484 p.

Ouimet, W.B., Whipple, K.X., and Granger, D.E., 2009, Beyond threshold hillslopes: Channel adjustment to base-level fall in tectonically active mountain ranges: Geology, v. 37, no. 7, p. 579–582, https://doi.org/10.1130/G30013A.1.

Perron, J.T., and Royden, L., 2013, An integral approach to bedrock river profile analysis: Earth Surface Processes and Landforms, v. 38, no. 6, p. 570–576, https://doi.org/10.1002/esp.3302.

Robertson, J., Meschis, M., Roberts, G.P., Ganas, A., and Gheorghiu, D.M., 2019, Temporally constant Quaternary uplift rates and their relationship with extensional upper-plate faults in South Crete (Greece), constrained with ^{36}Cl cosmogenic exposure dating: Tectonics, v. 38, p. 1189–1222, https://doi.org/10.1029/2018TC005410.

Roda-Boluda, D.C., and Whittaker, A.C., 2016, Normal fault evolution and coupled landscape response: Examples from the Southern Apennines, Italy: Basin Research, v. 28, no. 1, p. 1–24, https://doi.org/10.1111/bre.12215.

Rosenbloom, N.A., and Anderson, R.S., 1994, Hillslope and channel evolution in a marine terraced landscape, Santa Cruz, California: Journal of Geophysical Research, v. 99, no. B7, p. 14,013–14,029, https://doi.org/10.1029/94JB00048.

Pirazzoli, P., 2005, A review of possible eustatic, isostatic and tectonic contributions in eight late-Holocene relative sea-level histories from the Mediterranean area: Quaternary Science Reviews, v. 24, no. 18–19, p. 1989–2001, https://doi.org/10.1016/j.quascirev.2004.06.026.

Plaziat, J.-C., Purser, B.H., and Bosence, D.W.J., 1998, Quaternary marine and continental sedimentation in the northern Red Sea and Gulf of Suez (Egyptian coast): Influences of rift tectonics, climatic changes and sea-level fluctuations, in Purser, B.H., and Bosence, D.W.J., eds., Sedimentation and Tectonics in Rift Basins Red Sea–Gulf of Aden: Dordrecht, Springer Netherlands, p. 537–573, https://doi.org/10.1007/978-94-011-4930-3_29.

Schwanghart, W., and Scherler, D., 2014, TopoToolbox 2 – MATLAB-based software for topographic analysis and modeling in Earth surface sciences: Earth Surface Dynamics, v. 2, p. 1–7, https://doi.org/10.5194/esurf-2-1-2014.

Snyder, N.P., Whipple, K.X., Tucker, G.E., and Merritts, D.J., 2000, Landscape response to tectonic forcing: Digital elevation model analysis of stream profiles in the Mendocino triple junction region, northern California: GSA Bulletin, v. 112, no. 8, p. 1250–1263, https://doi.org/10.1130/0016-7606(2000)112<1250:LRTTFD>2.0.CO;2.

Stock, J., and Dietrich, W.E., 2003, Valley incision by debris flows: Evidence of a topographic signature: Water Resources Research, v. 39, no. 4, 1257, https://doi.org/10.1029/2001WR001057.

Tucker, G.E., and Whipple, K.X., 2002, Topographic outcomes predicted by stream erosion models: Sensitivity analysis and intermodel comparison: Journal of Geophysical Research, v. 107, no. B9, p. 2179, https://doi.org/10.1029/2001JB000162.

Whipple, K.X., 2004, Bedrock rivers and the geomorphology of active orogens: Annual Review of Earth and Planetary Sciences, v. 32, no. 1, p. 151–185, https://doi.org/10.1146/annurev.earth.32.101802.120356.

Whipple, K.X., and Tucker, G.E., 1999, Dynamics of the stream-power river incision model: Implications for height limits of mountain ranges, landscape response timescales, and research needs: Journal of Geophysical Research: Solid Earth, v. 104, no. B8, p. 17,661–17,674, https://doi.org/10.1029/1999JB900120.

Whittaker, A.C., 2012, How do landscapes record tectonics and climate?: Lithosphere, v. 4, no. 2, p. 160–164, https://doi.org/10.1130/RF.L003.1.

Whittaker, A.C., and Walker, A.S., 2015, Geomorphic constraints on fault throw rates and linkage times: Examples from the Northern Gulf of Evia, Greece: Journal of Geophysical Research: Earth Surface, v. 120, no. 1, https://doi.org/10.1002/2014JF003318.

Whittaker, A.C., Attal, M., Cowie, P.A., Tucker, G.E., and Roberts, G., 2008, Decoding temporal and spatial patterns of fault uplift using transient river long profiles: Geomorphology, v. 100, no. 3–4, p. 506–526, https://doi.org/10.1016/j.geomorph.2008.01.018.

Wobus, C., Whipple, K.X., Kirby, E., Snyder, N., Johnson, J., Spyropolou, K., Crosby, B., and Sheehan, D., 2006, Tectonics from topography: Procedures, promise, and pitfalls: Geological Society of America Special Papers, v. 398, p. 55–74, https://doi.org/10.1130/2006.2398(04).

Fernández-Blanco et al., Supplementary Material Figure A

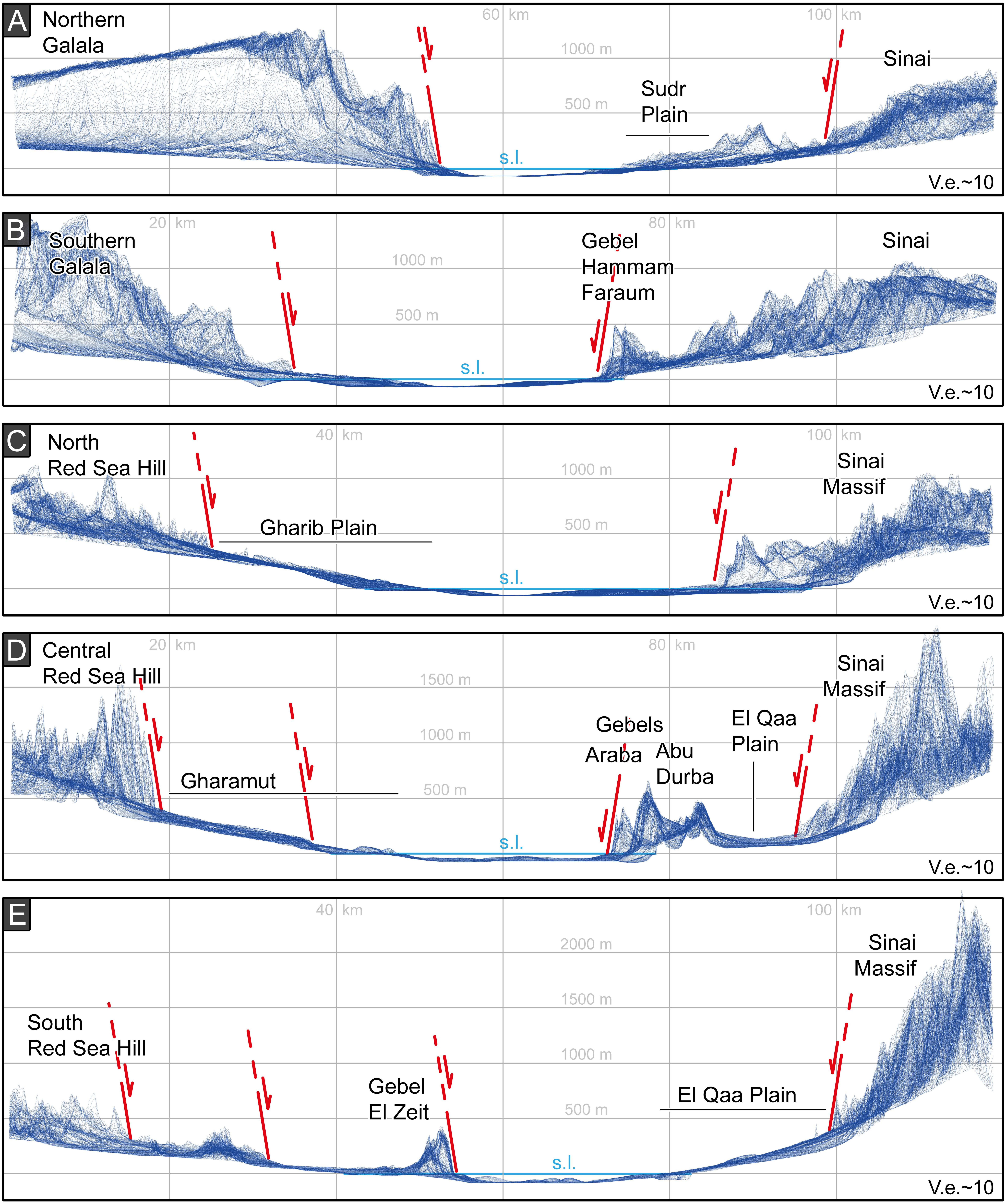

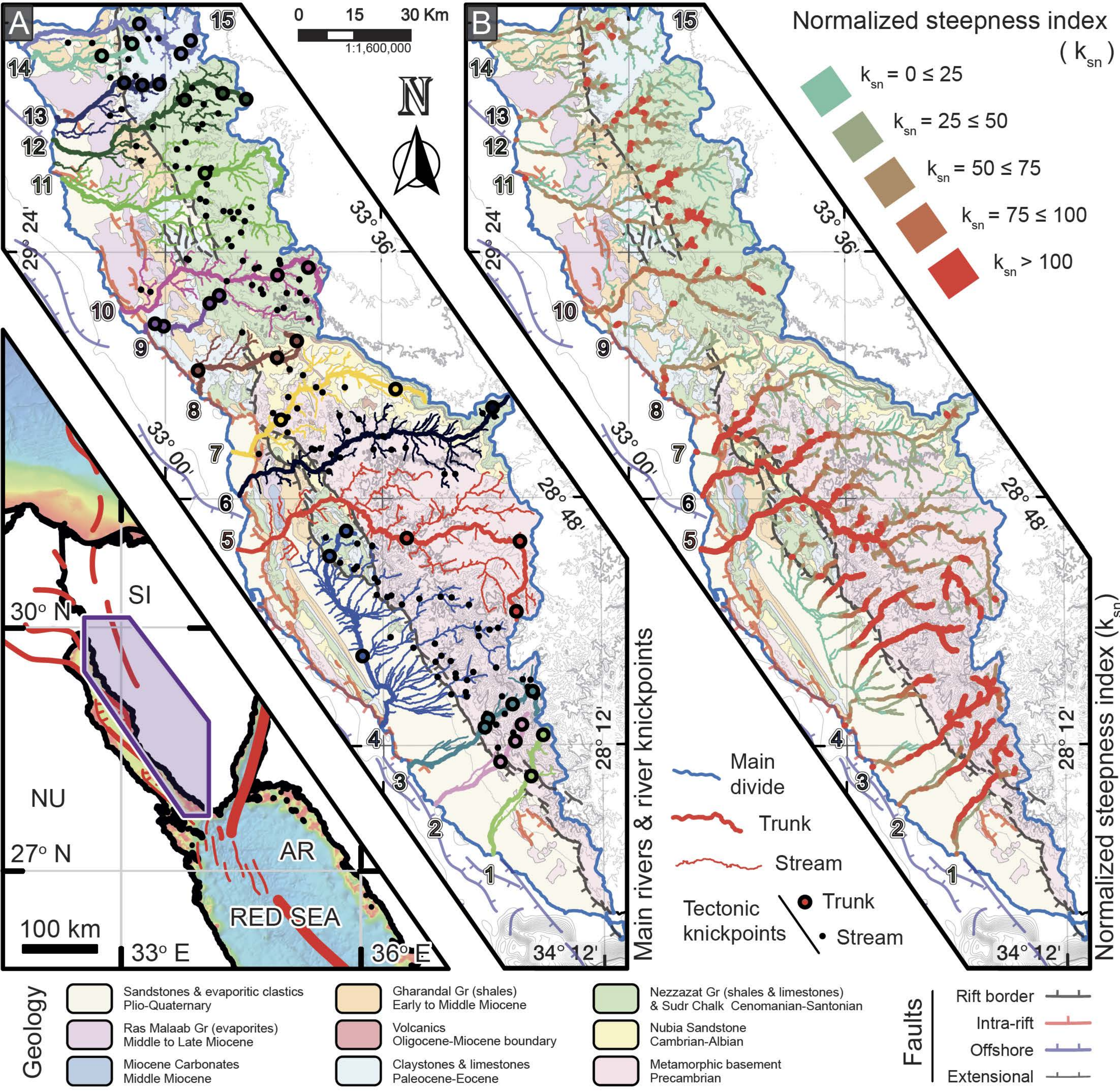

A
B
0 15 30 Km
1:1,600,000
N
Normalized steepness index
(k_{sn})
k_{sn} = 0 ≤ 25
k_{sn} = 25 ≤ 50
k_{sn} = 50 ≤ 75
k_{sn} = 75 ≤ 100
k_{sn} > 100
29° 24'
33° 36'
33° 00'
28° 48'
28° 12'
34° 12'
SI
30° N
NU
27° N
AR
RED SEA
100 km
33° E
36° E
Main rivers & river knickpoints
Main divide
Trunk
Stream
Tectonic knickpoints
Trunk
Stream
Normalized steepness index (k_{sn})
Geology
Sandstones & evaporitic clastics Plio-Quaternary
Ras Malaab Gr (evaporites) Middle to Late Miocene
Miocene Carbonates Middle Miocene
Gharandal Gr (shales) Early to Middle Miocene
Volcanics Oligocene-Miocene boundary
Claystones & limestones Paleocene-Eocene
Nezzazat Gr (shales & limestones) & Sudr Chalk Cenomanian-Santonian
Nubia Sandstone Cambrian-Albian
Metamorphic basement Precambrian
Faults
Rift border
Intra-rift
Offshore
Extensional

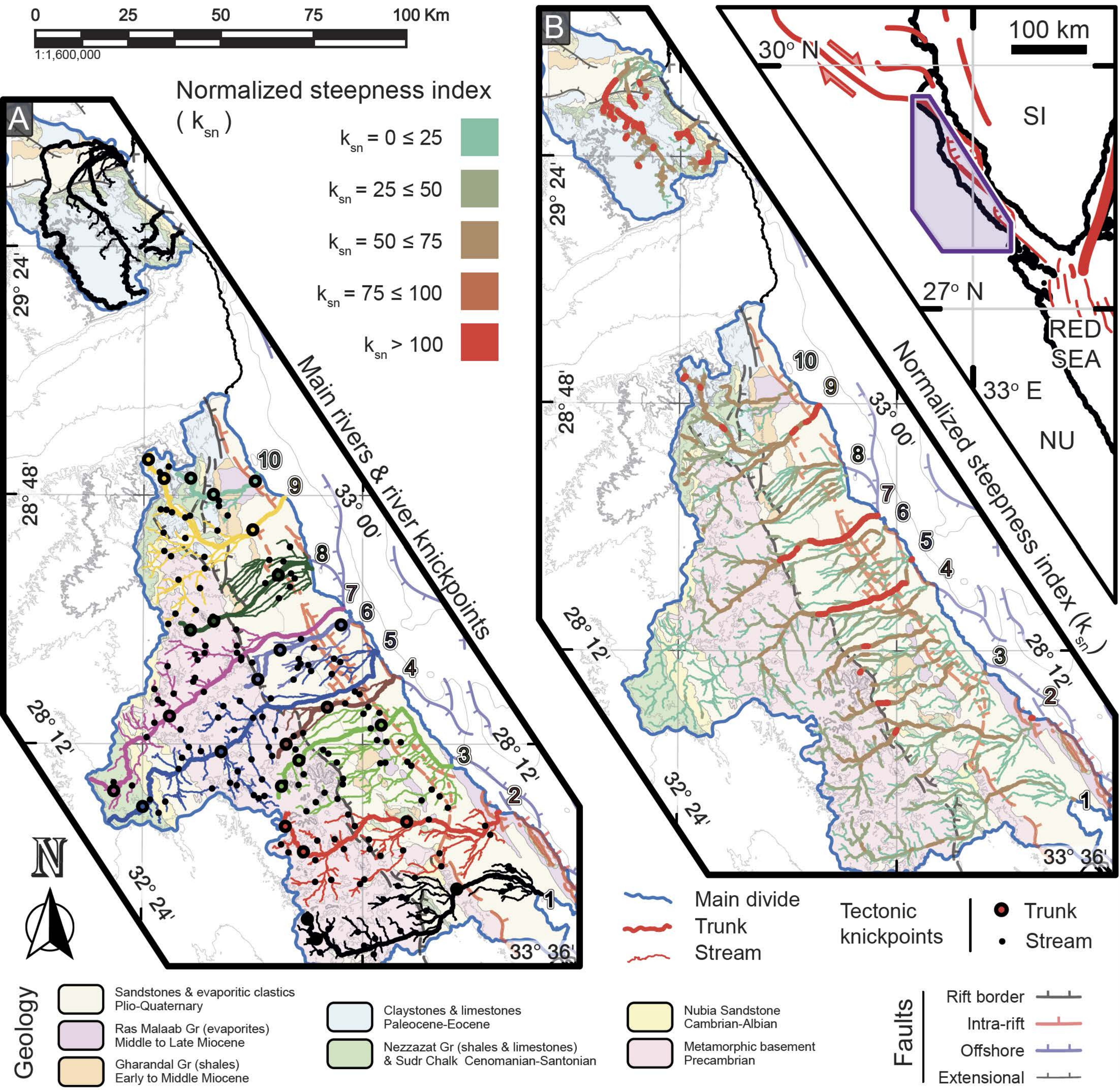

0 25 50 75 100 Km
1:1,600,000
Normalized steepness index
(k_{sn})
k_{sn} = 0 ≤ 25
k_{sn} = 25 ≤ 50
k_{sn} = 50 ≤ 75
k_{sn} = 75 ≤ 100
k_{sn} > 100
A
B
Main rivers & river knickpoints
Normalized steepness index (k_{sn})
29° 24'
28° 48'
28° 12'
33° 00'
32° 24'
33° 36'
30° N
27° N
33° E
100 km
SI
RED SEA
NU
Main divide
Trunk
Stream
Tectonic knickpoints
Trunk
Stream
Geology
Sandstones & evaporitic clastics Plio-Quaternary
Ras Malaab Gr (evaporites) Middle to Late Miocene
Gharandal Gr (shales) Early to Middle Miocene
Claystones & limestones Paleocene-Eocene
Nezzazat Gr (shales & limestones) & Sudr Chalk Cenomanian-Santonian
Nubia Sandstone Cambrian-Albian
Metamorphic basement Precambrian
Faults
Rift border
Intra-rift
Offshore
Extensional